ORIGINAL PAPER

Structural and Magnetic Studies of Annealed Iron Oxide Nanoparticles

M. Ounacer [1] · A. Essoumhi [1,2] · M. Sajieddine [1,3] · A. Razouk [1] · B. F. O. Costa [4] · S. M. Dubiel [5] · M. Sahlaoui [1]

Abstract

The aim of this research work was to study the structural and magnetic properties of iron oxide nanoparticles. The as-prepared sample was synthesized by a co-precipitation route and annealed at different temperatures. The annealed samples were investigated using different techniques such as X-ray diffraction (XRD), transmission electron microscopy (TEM), scanning electron microscopy (SEM), vibrating sample magnetometry (VSM), and Mössbauer spectrometry (MS). The XRD results indicate the formation of three phases which have been identified as magnetite (Fe_3O_4), maghemite (γ-Fe_2O_3), and hematite (a-Fe_2O_3). The crystallite size was very similar for both magnetite and maghemite, and it was higher for hematite. The TEM observations showed that the particle shapes were affected by the annealing temperature (T_{an}). In addition, the SEM analysis revealed a wide distribution of the particle size. The magnetic measurements enabled the determination of a blocking temperature for both Fe_3O_4 and γ-Fe_2O_3 as 210 and 240 K, respectively. The Morin transition temperature was determined in the case of α-Fe_2O_3 from the magnetization and the MS measurements. The synthesized iron oxide nanoparticles can be good candidates for hyperthermia applications.

Keywords Co-precipitation · Iron oxide nanoparticle · Rietveld refinement · XRD · TEM · Mössbauer spectrometry

1 Introduction

Iron oxide nanoparticles are materials that have been extensively studied in different laboratories. They are composed of many phases with particle size ranging from 1 to 100 nm [1]. The most known, as a natural and traditional magnetic material, is magnetite which can also be easily synthesized. However, the oxidation of magnetite occurs at very low temperature and leads to the formation of maghemite [2].

✉ M. Sajieddine
sajieddinem@yahoo.fr

1 Laboratoire de Physique des Matériaux, FST, Université Sultan Moulay Slimane, BP 523, 23000 Béni-Mellal, Morocco

2 Laboratoire des Procédés Chimiques et Matériaux Appliqués, FP, Université Sultan Moulay Slimane, 23000 Béni-Mellal, Morocco

3 National School of Applied Sciences, Sultan Moulay Slimane University, Khouribga, Morocco

4 CFisUC, Physics Department, University of Coimbra, Rua Larga, 3004-516 Coimbra, Portugal

5 Faculty of Physics and Applied Computer Science, AGH University of Science and Technology, al. A. Mickiewicza 30, 30-059 Kraków, Poland

Magnetite and maghemite have generated a very wide range of applications in several areas, especially in biomedicine. Because of their compatibility and suitability for in vivo applications, they were considered as good candidates for cancer therapy by hyperthermia, drug delivery, and magnetic resonance imaging [3–6], whereas hematite, another phase of iron oxides, is more stable, non-toxic, and corrosion resistant, and it has been used in lithium-ion batteries, pigments, gas sensors, and catalysts as well as in magnetic devices [7–10]. Magnetite possesses an inverse cubic spinel ferrite structure where both Fe^{3+} and Fe^{2+} ions occupy tetrahedral sites (B), and Fe^{3+} ions occupy octahedral sites (A), as indicated by the following formula: $(Fe^{3+})^A [Fe^{2+}Fe^{3+}]^B O_4$ [11]. The maghemite phase has similar characteristics as magnetite, whereas the structure of the former shows vacancies located on the B sites. The latter can be approximated by a cubic unit cell with the composition $(Fe^{3+})^A [Fe_{5/3}^{3+} \square_{1/3}]^B O_4$; the square presents a vacuum in B site, which is also known as γ-Fe_2O_3 [12]. According to previous studies reported in the literature, it is difficult to distinguish between magnetite and the maghemite due to their similar structural and magnetic properties. The main difference between maghemite and magnetite is their chemical stability [1]. Hematite, α-Fe_2O_3, crystallizes in the hexagonal corundum structure [13]. The hematite phase

shows an exceptional magnetic behavior that appears below the Néel temperature (T_N = 960 K). Indeed, it shows a transition from an antiferromagnetic state at low temperature to a weak ferromagnetic state at room temperature. This transition is called the Morin transition and it occurs at the Morin temperature, T_M = 264 K, for the bulk [14]. For particles, T_M is smaller and decreases with the average size of grains, D [14]. Various synthesis methods of iron oxide materials have been reported in the literature such as hydrothermal [15, 16], solvothermal [17], microwave [18], sol–gel [19], flash autocombustion, and mechanosynthesis [20, 21]. Among all these methods, the chemical co-precipitation route is the most commonly used to produce magnetic nanoparticles due to its easiness, low cost, and production of homogenous samples.

In this paper, we present our contribution to the issue by studying the annealing effect on the iron oxide synthesized by a simple chemical co-precipitation route. To investigate our samples, structural characterizations were carried out by using X-ray diffraction (XRD), scanning electron microscopy (SEM), and transmission electron microscopy (TEM). Moreover, magnetic properties were studied by using the vibrating sample magnetometer (VSM) at both low and room temperatures. The zero-field-cooled (ZFC) and field-cooled (FC) measurements were also performed. The study was supplemented by Mössbauer spectrometry (MS) measurements.

2 Experimental

2.1 Synthesis Method

The synthesis of iron oxide nanoparticles was carried out by the co-precipitation route [22–24]. Ferric chloride ($FeCl_3 \cdot 6H_2O$) (Alfa Aesar), ferrous sulfate ($FeSO_4 \cdot 7H_2O$) (Alfa Aesar), and sodium hydroxide (NaOH) from VWR were used as raw materials. All the chemicals were used as received. Appropriate masses of iron salts with the ratio of Fe^{3+}/Fe^{2+} equal to 2:1 were dissolved in distilled water. This solution was added to NaOH (100 ml, 1 M) solution whose pH and
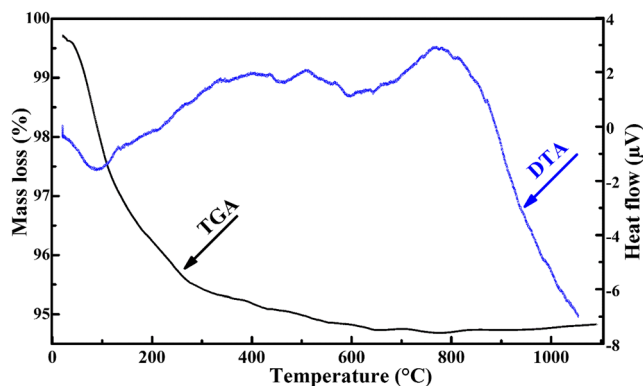
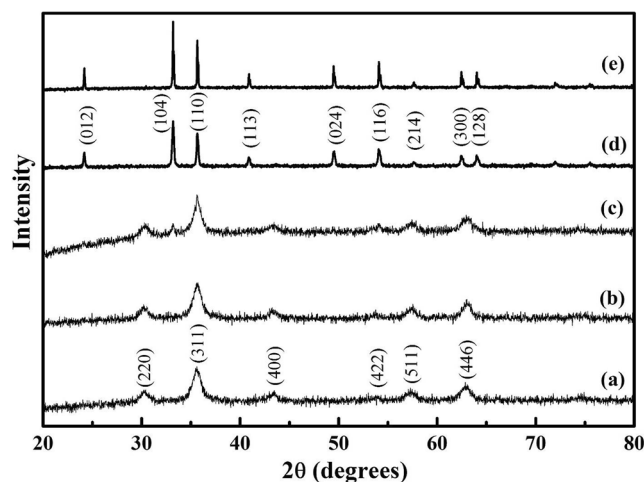**Fig. 1** TG–DTA curves for the as-prepared sample

Fig. 2 X-ray diffraction patterns collected at room temperature for the as-prepared (**a**) and annealed samples; 250 (**b**), 450 (**c**), 650 (**d**), and 850 °C (**e**)

temperature were fixed at 12 and 70 °C, respectively. A black solution was formed immediately showing that the formation of iron oxide nanoparticles in the colloidal suspension took place. The obtained solution was kept under agitation for 30 min, then the precipitated product was filtered out, washed with distilled water several times, and finally dried in an oven at 60 °C overnight. The resulting product was ground into powder and then annealed in a muffle furnace for 2 h.

2.2 Characterization Techniques

A thermogravimetric analyzer (LabSys EVO Setaram 1600) was used to investigate thermal changes in the as-prepared sample. Based on the analysis of GT-DTA curves, different annealing temperatures, namely, 250, 450, 650, and 850 °C, were chosen. A phase identification of the samples was performed by an X-ray diffractometer (Bruker, D8-Advance) in the reflection mode, using CuK_α radiation (λ = 1.5406 Å). Diffraction patterns were collected in the 2θ range from 20° to 80°. Mean crystallite sizes of the samples were estimated by using Scherrer's formula $D = k\lambda/\Delta(2\theta)\cos\theta$ [25], where D is a mean crystallite size, k is an instrumental constant of 0.9, θ is a Bragg angle, and $\Delta(2\theta)$ is a half intensity width of the relevant diffraction peak. X-ray density was defined by the formula $\rho = 8\ M/VN$ [26], where M is the relative molecular mass, V is the volume of unit cell (in case of cubic system, $V = a^3$), and N is Avogadro's constant.

The XRD data were also used for refining the lattice parameters by using the *Bruker-Diffract*.EVA software [27]. Also, the XRD data of each sample were refined with the help of the Fullprof software using the Rietveld method [28] in two steps. First, the profile-matching step through which the global parameters such as factor scale, lattice parameters, zero, background, profile shape, asymmetry parameters, and preferred orientation parameters were fitted. In the second step,
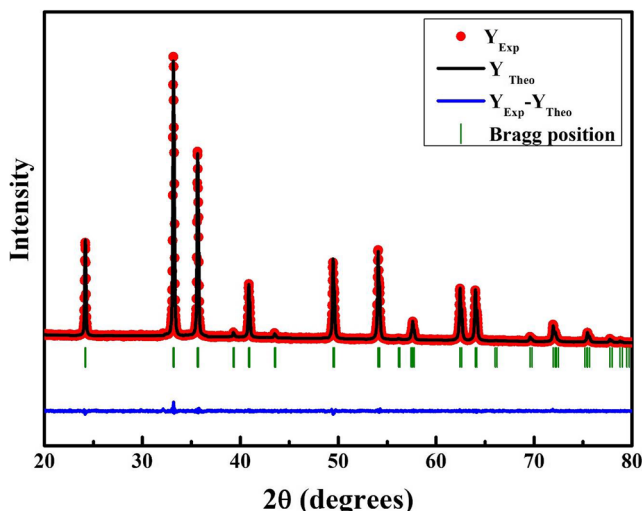
Fig. 3 Rietveld refinement on the hematite sample with a space group Rc-3

the atomic coordinates, isothermal parameters, and site occupancies were refined in the structural model. The obtained parameters such as χ^2 (goodness of fit) and the R factors (R_p the profile factor, R_{wp} the weighted residual factor, R_B the Bragg factor, and R_F the crystallographic factor) were used to confirm the fit quality of the experimental data. The micrographs were obtained by SEM (VEGA-3 SBH TESCAN). Morphology of the powders was investigated by a transmission electron microscope (TECNAI G^2). To do this, a small amount of powder was milled in acetone and then placed in an ultrasonic bath to disperse the nanoparticles. A drop of this solution was then placed on a copper grid covered with carbon which was spontaneously dried in air. Purity of the samples and the verification of the chemical composition were done by X-ray microanalysis. Magnetization measurements were carried out using the vibrating sample magnetometer (VSM). The hysteresis loops were measured at various temperatures (1.8, and 300 K) with an applied magnetic field up to 9 T. Thermal

variation of zero-field-cooled (ZFC) and field-cooled (FC) measurements were carried out under a small applied magnetic field of 100 Oe. ^{57}Fe Mössbauer spectra were collected using a 25 mCi ^{57}Co source in a Rh matrix in a constant acceleration mode using a standard transmission configuration of a Mössbauer spectrometer (Wissel GmbH). The hyperfine parameters, magnetic hyperfine field (H_{hyp}), isomer shift (IS), quadrupole splitting (ΔEQ), relative area (A), and line width (Γ) were determined by fitting the spectra with the NORMOS program. The velocity scale was calibrated using a α-Fe foil at 300 K and the values of the isomer shifts are given relative to this standard.

3 Results and Discussion

3.1 Thermal Studies

The TG-DTA analysis was performed to investigate the weight loss during the heat treatment of the as-prepared sample. Figure 1 shows the GT-DTA curves. As we can see, the first loss occurred at temperatures below 200 °C, and it can be associated with evaporation of water absorbed on particles' surfaces. In addition, for 200 °C $\leq T \leq$ 600 °C, we note a weak weight loss that can be attributed to the removal of anions such as OH^-, Cl^-, and sulfate anions that had remained after the washing process. It is worth indicating that no loss of weight can be observed above 800 °C in the TGA curve, while a broad exothermal peak appeared at ~850 °C in the DTA curve. The latter means that an iron oxide phase was formed at this temperature. Furthermore, the DTA curve reveals endothermic peaks in the temperature range of 200–700 °C. Thus, in order to get more insight into the phenomena reflected by the thermal behavior, the as-prepared sample was annealed at different temperatures (T_{an} = 250, 450, 650, and 850 °C).

Table 1 Values of Rietveld factors as well as structural parameters of magnetite, maghemite, and hematite

| Parameters		Samples		
		Magnetite: Fe_3O_4	Maghemite: γ-Fe_2O_3	Hematite: α-Fe_2O_3
Rietveld factors	R_p (%)	74	77.7	8.77
	R_{wp} (%)	38.9	38.3	5.06
	R_F (%)	4.3	9.2	0.86
	R_B (%)	4.8	4.7	0.64
	χ^2	0.67	0.67	0.93
Structural parameters	a (Å)	8.3521	8.3389	5.035
	c (Å)	–	–	13.748
	V (Å^3)	582.6	579.8	301.8
	ρ (g/cm^3)	4.89	7.89	5.38
	D (nm)	8.0	8.1	70.0

Table 2 Atoms, Wyckoff positions, atom positions, and occupancy for each of magnetite, maghemite, and hematite

| Sample	Atom	Wyckoff position	x	y	z	Occupancy
Hematite	Fe^{3+}	12c	0	0	0.3553	0.312
	O^{2-}	18e	0.3068	0	0.2500	0.500
Maghemite	Fe^{3+}	4b	7/8	7/8	7/8	0.11
	Fe^{3+}	12d	1/8	7/8	1/8	0.47
	Fe^{3+}	8c	1/2	1/2	1/2	0.33
	$O^{2-}(1)$	24e	1/8	1/8	5/8	1.00
	$O^{2-}(2)$	8c	5/8	5/8	5/8	0.40
Magnetite	Fe^{3+}	16d	1/2	1/2	1/2	1.05
	Fe^{3+}	8a	1/8	1/8	1/8	0.95
	Fe^{2+}	16d	1/2	1/2	1/2	0.95
	F^{e2+}	8a	1/8	1/8	1/8	0.05
	O^{2-}	32e	0.2563	0.5263	0.2563	4

3.2 Structural and Morphological Analysis

The XRD patterns are presented in Fig. 2 for all studied samples. By identifying the Bragg positions (2θ) with the Crystallography Open Database (COD) files that were included into the indexation "*BRUKER_Diffract.EVA*" program, the as-prepared sample was identified as the magnetite (Fe_3O_4) phase. The pattern of the sample calcined at 850 °C revealed characteristic peaks of the hematite phase (α-Fe_2O_3). It is well known that the magnetite can be easily converted to maghemite (γ-Fe_2O_3) in the range of temperature from 200 to 300 °C [29], and the XRD patterns are similar for both oxides. In fact, there is a slight shift in Bragg positions, which means a reduction of a cell parameter "a." Indeed, the cell parameter of a bulk magnetite ($a = 8.396$ Å) is larger than the one of a bulk maghemite (8.346 Å) [30]. Noteworthy, maghemite and magnetite can be easily distinguished from each other by their colors; magnetite is black while maghemite
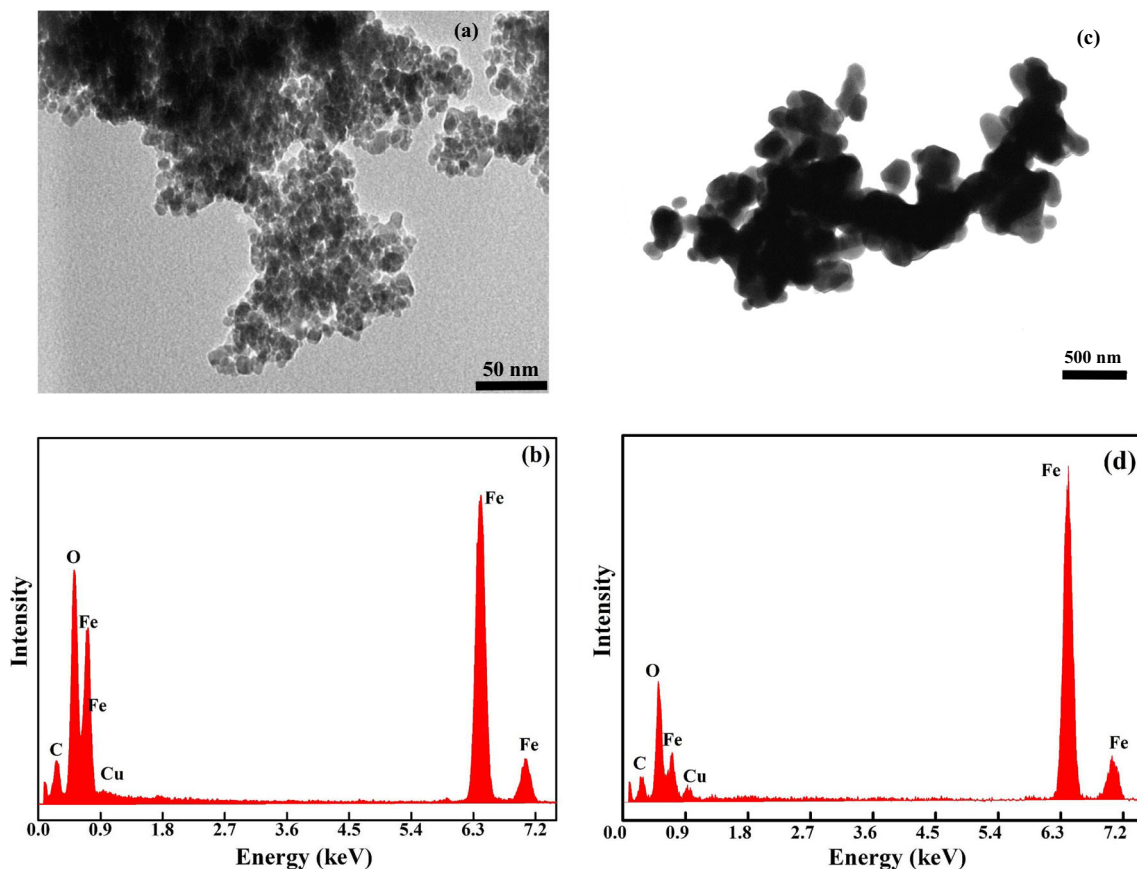

Fig. 4 TEM images and the respective microanalysis X for the maghemite (**a**, **b**) and the hematite (**c**, **d**)
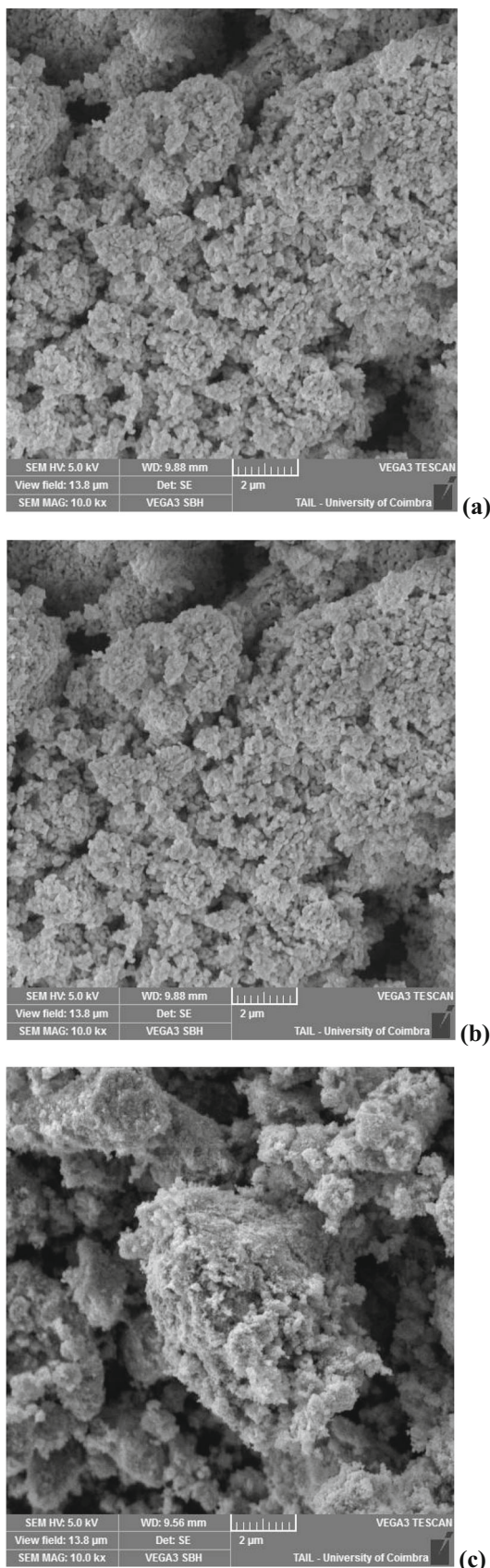
Fig. 5 SEM micrographs of the identified phases: magnetite (**a**), maghemite (**b**), and hematite (**c**)

is brown [31]. These iron oxides crystallize in a cubic system while hematite has a rhombohedral unit cell. Both maghemite and hematite were obtained by the oxidation treatment of the as-prepared magnetite phase in line with Eqs. (1) and (2) [29]:

$$2Fe_3O_4 + 0.5O_2 \rightarrow 3\gamma\text{-}Fe_2O_3 \tag{1}$$

$$2Fe_3O_4 + 0.5O_2 \rightarrow 3\alpha\text{-}Fe_2O_3 \tag{2}$$
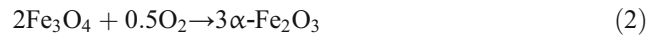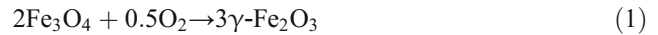
In order to further verify the phases and get access to additional structural parameters, Rietveld refinement was carried out on the as-prepared sample (magnetite), the one calcined at 250 °C (maghemite) as well as that calcined at 850 °C (hematite) with space groups F*d-3m*, P*4₃32*, and R-*3c:H*, respectively. A typical refinement of the hematite phase is shown in Fig. 3, while the structural parameters of each pattern as well as the refinement factors including the goodness of fit, χ^2, are displayed in Table 1. It can be seen that the cell parameter of the sample calcined at 250 °C is equal to 8.3389 Å which is very close to the one of the maghemite phase. The pseudo-Voigt profile was used when fitting the full width at half maximum ($\Delta(2\theta)$). This procedure yielded the average crystallite size to be 8 nm for both magnetite and maghemite particles, and 70 nm for hematite particles. Atom positions as well as their occupancies were obtained, too (Table 2). In order to verify homogeneity of the samples, TEM observations were performed and the obtained images are shown in Fig. 4. As we can see in Fig. 4a, the shapes of the nanoparticles are almost spherical but not homogeneous. By increasing the annealing temperature up to 850 °C, they change their shape and present irregular forms (Fig. 4c). The nanoparticle sizes increase with the annealing temperature in agreement with the XRD analysis. The chemical composition of the samples was checked based on the EDS spectra obtained along with the TEM image. Figure 4b and d shows the resulting EDS spectra where Fe and O peaks are clearly seen. Copper and carbon peaks, present in the spectra, are attributed to the grid used for the TEM observation of the samples. The morphology of the ferrite powders was also investigated using the SEM analysis. Figure 5 shows SEM micrographs of magnetite (Fig. 5a), maghemite (Fig. 5b), and hematite (Fig. 5c). One can see a wide distribution of the particle size, which is a characteristic of all samples.

3.3 Magnetic Studies

3.3.1 VSM Measurements

Hysteresis cycles *M(H)* for the magnetite, maghemite, and hematite samples are displayed in Fig. 6. The magnetite and maghemite samples present a similar magnetic behavior with a slight difference in their magnetic parameters at 1.8 and 300 K due to their chemical compositions and crystallite sizes

Fig. 6 Hysteresis loops measured
at 1.8 and 300 K for magnetite
(**a**), maghemite (**b**), and hematite
(**c**) samples
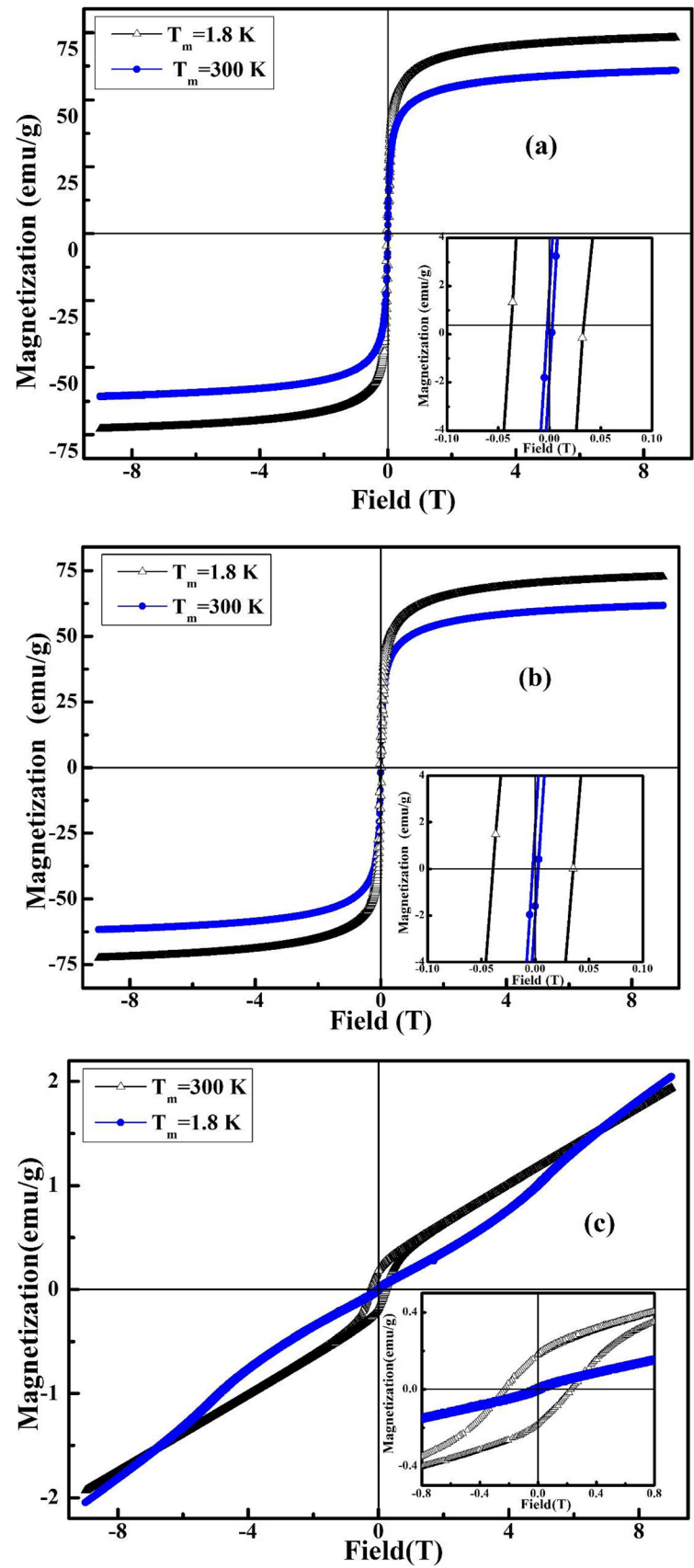
(Table 3). For each sample, the saturation magnetization (M_s) increases from 60 to 70 emu/g when the temperature decreases. In addition, the coercive field (H_c) is close to zero at room temperature, reflecting thereby a superparamagnetic character of both magnetite and maghemite nanoparticles. Such behavior is in good agreement with the results of Upadhyay et al. [32] that predict superparamagnetic behavior for nanoparticles smaller than a critical size of 14 nm. At 1.8 K, the coercive field increased for both oxides that can be interpreted in terms of a ferrimagnetic behavior below the blocking temperature T_B as indicated in the inset of Fig. 6a and b. The hysteresis loop of hematite reveals a weak ferromagnetic (WF) state at 300 K without any saturation (Fig. 6c). The value determined for the coercive field H_c is among the highest values reported in the literature for this compound ($H_c = 2270$ Oe), which is significantly larger than the value found for the bulk hematite ($H_c \approx 1670$ Oe) [33]. For comparison, the H_c value reported in the present work is close enough to that found by Tadic et al. (2340 Oe), whereas the coercivity (H_c) varies from 73 to 2688 Oe depending on the shape and size of the hematite nanoparticles [34, 35]. Also, we note that the hysteresis loop measured at 1.8 K for hematite shows an antiferromagnetic (AF) behavior. The observed transition between the AF and WF states can be associated with magnetic phenomena that are discussed below.

The temperature dependence of the ZFC–FC magnetization curves of magnetite and maghemite show a ferrimagnetic state below the blocking temperature (T_B) of 210 and 240 K, respectively. The value of the irreversibility temperature (T_{irr}) was estimated as 240 and 296 K for magnetite and maghemite, respectively (see inset of Fig. 7a and b). The knowledge of this temperature allows getting information on the grain size distribution. As known, in the ideal non-interacting monodispersed nanoparticles, T_{irr} and T_B values are compared [32]. According to Jacob et al. [36], the difference between T_{irr} and T_B ($T_{irr} - T_B$) determines the width of the blocking temperatures which in our case correspond to 30 and 56 K for magnetite and maghemite, respectively. As ($T_{irr} - T_B$) in the present case, which is not large, one may assume that the nanoparticles are monodispersed. T_B is known to be proportional to the anisotropy, hence it follows that the maghemite particles would have higher anisotropy than the magnetite particles as they have the same D value. Above T_B, both

magnetite and maghemite show a superparamagnetic behavior known by the lack of coercivity (see Fig. 7a and b). As it can be seen, the FC curves display no evolution of magnetization for both magnetite and maghemite for $T < T_B$. This kind of behavior is a particular feature of interacting nanoparticles. Aslibeiki et al. [37] has claimed that the inter-particle interactions were concluded from a flat character of magnetization depicted in FC curve for $T < T_B$. The ZFC–FC curves of the hematite present a non-common magnetic phase well known by a spin-flop transition or the Morin transition. The latter indicates a transition from an antiferromagnetic state at low temperature ($< T_M$, T_M is the Morin temperature), where spins reorganize perpendicularly to the c-axis of the hematite structure, to a weak ferromagnetic state observed at 300 K, in which the spins are arranged along the c-axis. Following Jacob et al. [36], T_M was estimated to be 230 K—the average value obtained from the FC and ZFC curves (Fig. 7c). This magnetic phase transition, as a characteristic magnetic property of hematite nanoparticles, depends on various factors especially on the degree of crystallinity, size and shape of nanoparticles, heat treatment, and synthesis method [36, 38, 39]. In particular, its dependence on the size of grains, D, can be described by the following formula [14]:

$$T_M(D) = 264\left(1 - \frac{8.3}{D}\right) \tag{3}$$

where 264 (K) is the Morin temperature of the bulk and D (nm) is the mean particle size. Using this formula for our case ($D = 70$ nm) gives $T_M = 232.7$ K, a figure which agrees well with the one determined from the magnetization measurements, i.e., 230 K.

3.3.2 Mössbauer Measurements

Room-temperature Mössbauer spectra of both magnetite and maghemite samples are exhibited in Fig. 8a and b, respectively. As we can see, the spectrum of both samples is magnetically split, but lines are very broad. This can be understood in terms of a distribution of the hyperfine field. As the samples are superparamagnetic due to small particle sizes, the distribution is caused by a relaxation of magnetic moments at 300 K. The spectrum of the magnetite could have been successfully

Table 3 Magnetic parameters (M_s, M_r, and H_c) at 1.8 and 300 K of magnetite, maghemite, and hematite

| Sample	$T_M = 1.8$ K			$T_M = 300$ K		
	M_s (emu/g)	M_r (emu/g)	H_c (T)	M_s (emu/g)	M_r (emu/g)	H_c (T)
Magnetite	73.0	18.01	0.030	60.8	1.6	0.002
Maghemite	72.1	22.70	0.050	61.7	13.3	0.036
Hematite	–	0.01	0.010	–	0.2	0.227

The meaning of the symbols is given in the text

Fig. 7 ZFC and FC magnetization curves of magnetite (**a**), maghemite (**b**), and hematite (**c**). The blocking and the irreversibility temperature, T_B and T_{irr} are indicated in the inset of (**a**) and (**b**)
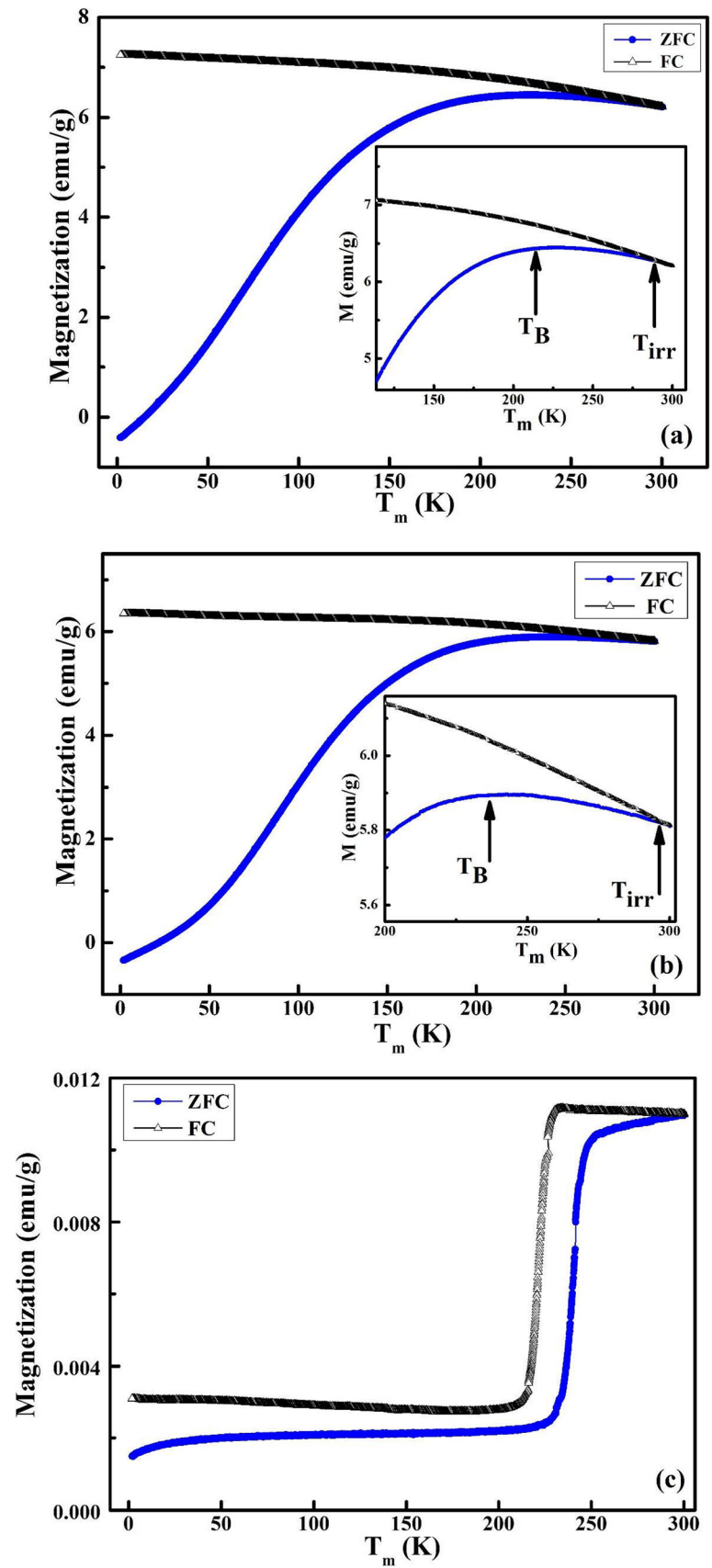
Fig. 8 ^{57}Fe Mössbauer spectra collected at room temperature for magnetite (**a**) and maghemite (**b**)
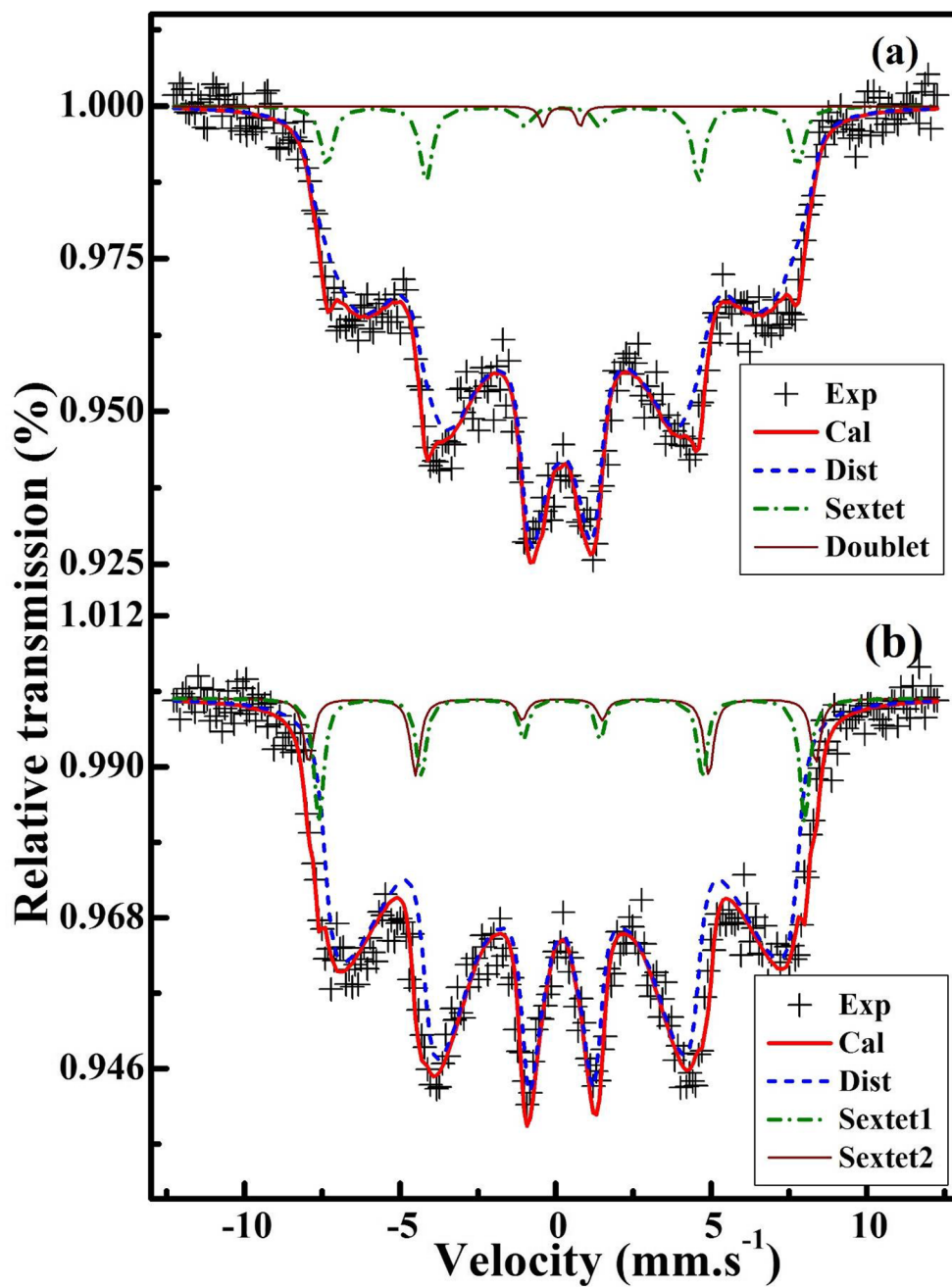

Table 4 Room-temperature hyperfine spectral parameters for magnetite and maghemite

Samples	Subspectrum	A (%)	H_{hyp} (T)	IS (mm/s)	ΔEQ (mm/s)	Γ (mm/s)
Magnetite	Sextet	5	47.00	0.36	–	0.48
	Doublet	1	–	0.34	1.2	0.28
	Distribution	94	29.0	0.31	–	0.54
Maghemite	Sextet 1	4	50.62	0.36	–	0.38
	Sextet 2	6	48.50	0.35	–	0.38
	Distribution	90	32.10	0.29	–	0.55

The meaning of the parameters is described in the text

Fig. 9 ^{57}Fe Mössbauer spectra of hematite collected at various measured temperatures: 300 (**a**), 80 (**b**), and 6 K (**c**)
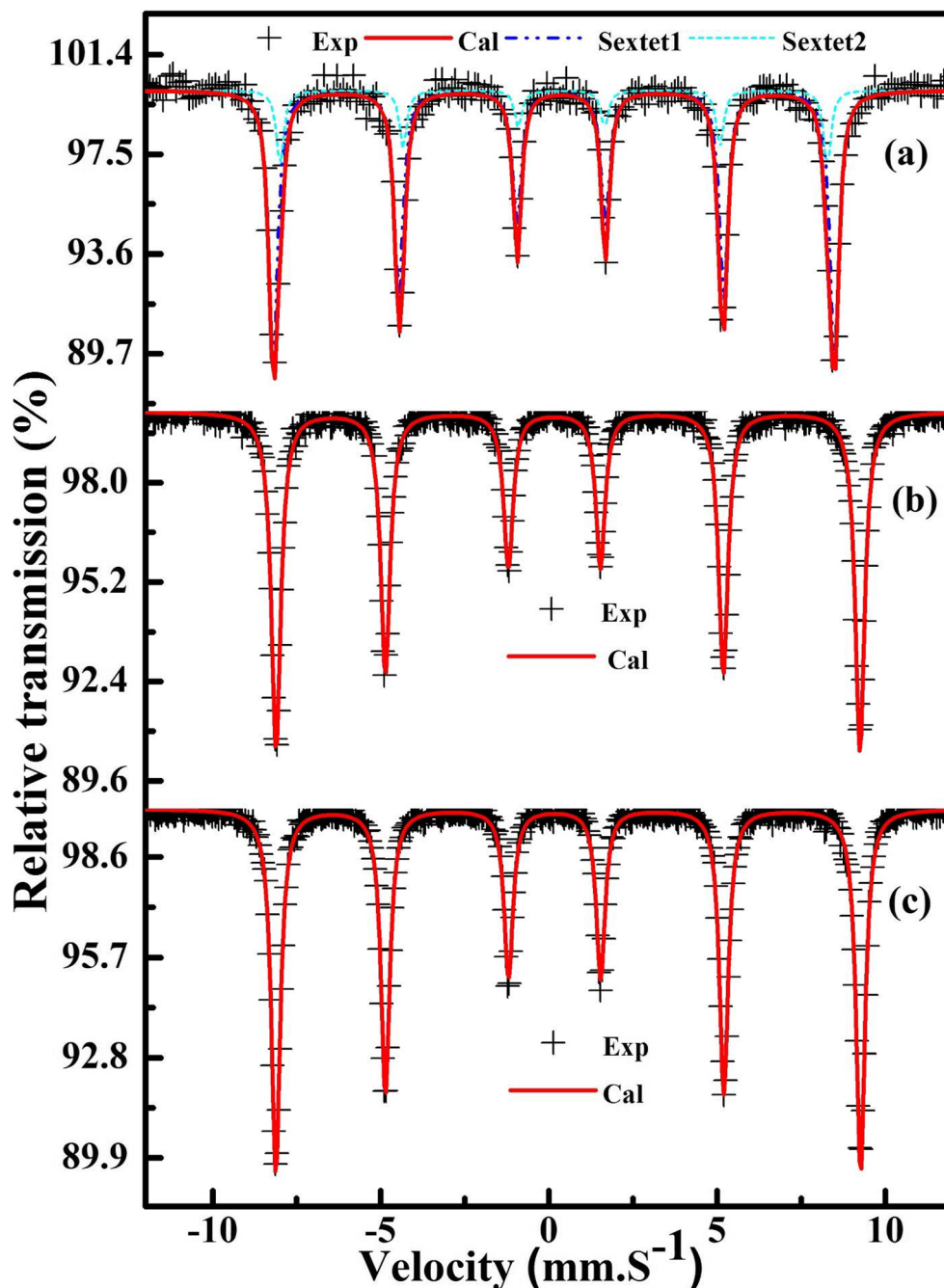

fitted in terms of a superposition of one distribution of the hyperfine field plus one sextet and one doublet. In the case of the maghemite, the spectrum has been well fitted in a similar way but using two sextets and a broad distribution. The hyperfine parameters obtained for both samples are displayed in Table 4. Therefore, the Mössbauer spectrum of

Table 5 Hyperfine spectral parameters of hematite related to the spectra measured at 300, 80, and 6 K

T_M (K)	Subspectrum	A (%)	H_{hyp} (T)	IS (mm/s)	ΔEQ (mm/s)	Γ (mm/s)
300	Sextet 1	81	51.1	0.37	− 0.11	0.30
	Sextet 2	19	50.4	0.37	− 0.12	0.25
80	Sextet	100	53.8	0.51	0.20	0.30
6	Sextet	100	53.8	0.51	0.20	0.30

Fig. 10 Dependence of the average hyperfine field, $\langle H_{hyp} \rangle$, at room temperature versus annealing temperature, T_{an}. The line was drawn as a guide to the eyes
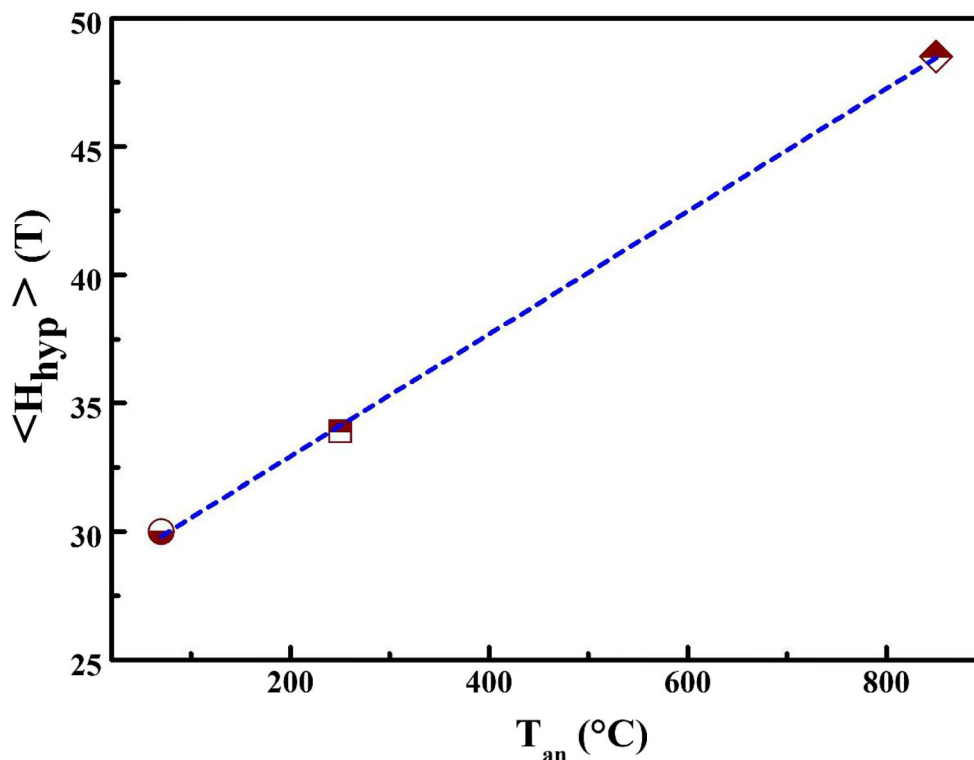
hematite exhibits narrow peaks that give evidence of its good crystallinity which is in line with the X-ray results. It is well known that the hematite presents a hexagonal structure with a single iron site (Fe^{3+}) in its crystal lattice that would normally be represented by one sextet at 300 K. However, in our case, the spectrum of hematite had to be analyzed by a superposition of two sextets (Fig. 9a). The calculated hyperfine parameters of both subspectra are listed in Table 5. The principal sextet with higher area ($\sim 81\%$) and H_{hyp} equal to 51.1 T can be attributed to a bulk hematite phase [36]. The presence of the secondary sextet with a smaller spectral area ($\sim 19\%$) and H_{hyp} of 50.4 T can be related to a surface effect of iron ions at 300 K. In other words, the two sextets are attributed to Fe atoms occupying the inner part (core) of the nanoparticles and iron atoms present on or near their surfaces. Mössbauer spectra of the hematite were also recorded at 80 and 6 K (Fig. 9b, c) in order to highlight the presence of the Morin transition as a typical magnetic feature of the hematite nanoparticles. The Mössbauer technique has been considered as a powerful tool to study this magnetic behavior via a quadrupole splitting (ΔEQ) parameter. Indeed, a negative value of ΔEQ at 300 K is indicative of a weak ferromagnetic behavior [40]. The analysis of the spectra collected at 80 and 6 K gave a positive ΔEQ that indicates an antiferromagnetic state of the hematite and confirms the magnetic results. Figure 10 illustrates the evolution of the average magnetic hyperfine field, $\langle H_{hyp} \rangle$, versus the annealing temperature. We can see that $\langle H_{hyp} \rangle$ increases linearly with temperature from 30 (magnetite) to 48.5 T (hematite).

4 Summary

Magnetite nanoparticles were synthesized by a co-precipitation method in given conditions of pH and temperature. To study the effect of annealing on structural and magnetic properties of the samples, XRD, TEM, SEM, VSM, and Mössbauer spectrometry techniques were used. The XRD results indicated that the as-prepared sample was identified as magnetite (Fe_3O_4) phase. It was changed to maghemite (γ-Fe_2O_3) by annealing at 250 °C and to hematite (α-Fe_2O_3) by annealing at 850 °C. Using the Rietveld refinement, the average crystallite sizes were determined: they were very similar for both magnetite and maghemite (8 nm), while for the hematite the value of 70 nm was determined. TEM and SEM microscopic observations confirmed the increase of nanoparticle sizes revealing a wide distribution of the size of the nanoparticles for all the samples. In addition, TEM images gave evidence that the shape of the nanoparticles transformed from spherical nanoparticles to nanoparticles with irregular forms as a function of the annealing temperature. The blocking temperature was estimated as 210 and 240 K for magnetite and maghemite, respectively. Regarding hematite, a non-common magnetic transition from a weak ferromagnet to antiferromagnet, known as the Morin transition, was evidenced. The spectral hyperfine parameters deduced from the measured Mössbauer spectra recorded for each sample allowed us to conclude that the magnetite and maghemite nanoparticles exhibited similar magnetic behaviors, and that hematite had a weak ferromagnetic state which changed to an

antiferromagnetic one at low temperatures, less than the Morin temperature, which was determined as 230 K.

References

1. Can, M.M., Coskun, M., Fırat, T.: A comparative study of nanosized iron oxide particles; magnetite (Fe_3O_4), maghemite (γ-Fe_2O_3) and hematite (a-Fe_2O_3) using ferromagnetic resonance. J. Alloys Compd. **542**, 241–247 (2012)

2. Sun, Y., Ma, M., Zhang, Y., Gu, N.: Synthesis of nanometer-size maghemite particles from magnetite. Colloids Surf. A Physicochem. Eng. Asp. **245**, 15–19 (2004)

3. Oh, J.K., Park, J.M.: Iron oxide-based superparamagnetic polymeric nanomaterials: design, preparation, and biomedical application. Prog. Polym. Sci. **36**, 168–189 (2011)

4. Gupta, A.K., Gupta, M.: Synthesis and surface engineering of iron oxide nanoparticles for biomedical applications. Biomaterials. **26**, 3995–4021 (2005)

5. Guo, S., Li, D., Zhang, L., Li, J., Wang, E.: Monodisperse mesoporous superparamagnetic single-crystal magnetite nanoparticles for drug delivery. Biomaterials. **30**, 1881–1889 (2009)

6. Liu, X., Tao, Y., Mao, H., Kong, Y., Shen, J., Deng, L., Yang, L.: Construction of magnetic-targeted and NIR irradiation-controlled drug delivery platform with Fe3O4@au@SiO2 nanospheres. Ceram. Int. **43**, 5061–5067 (2017)

7. Haw, C.Y., Mohamed, F., Chia, C.H., Radiman, S., Zakaria, S., Huang, N.M., Lim, H.N.: Hydrothermal synthesis of magnetite nanoparticles as MRI contrast agents. Ceram. Int. **36**, 1417–1422 (2010)

8. Zhang, L., Wu, H.B., Lou, X.W., Iron-oxide-based advanced anode materials for lithium-ion batteries, Adv. Energy Mater. **4** (2014) 1–11

9. Wu, C., Yin, P., Zhu, X., Yang, C.O., Xie, Y.: Synthesis of hematite (α-Fe_2O_3) nanorods: diameter-size and shape effects on their applications in magnetism, lithium ion battery, and gas sensors. J. Phys. Chem. B. **110**, 17806–17812 (2006)

10. Yanyan, X., Shuang, Y., Guoying, Z., Yaqiu, S., Dongzhao, G., Yuxiu, S.: Uniform hematite α-Fe_2O_3 nanoparticles: morphology, size-controlled hydrothermal synthesis and formation mechanism. Mater. Lett. **65**, 1911–1914 (2011)

11. Fleet, M.E.: The structure of magnetite: symmetry of cubic spinels. J. Solid State Chem. **62**, 75–82 (1986)

12. Shokrollahi, H.: A review of the magnetic properties, synthesis methods and applications of maghemite. J. Magn. Magn. Mater. **426**, 74–81 (2017)

13. Rollmann, G., Rohrbach, A., Entel, P., Hafner, J.: First-principles calculation of the structure and magnetic phases of hematite. Phys. Rev. B. **69**, 1–12 (2004)

14. Amin, N., Arajs, S.: Morin temperature of annealed submicronic α-Fe_2O_3 particles. Phys. Rev. B. **35**, 4810–4811 (1987)

15. Sato, J., Kobayashi, M., Kato, H., Miyazaki, T., Kakihana, M.: Hydrothermal synthesis of magnetite particles with uncommon crystal facets. J. Asian Ceram. Soc. **2**, 258–262 (2014)

16. Chen, Z., Du, Y., Li, Z., Yang, K., Lv, X.: Controllable synthesis of magnetic Fe_3O_4 particles with different morphology by one-step hydrothermal route. J. Magn. Magn. Mater. **426**, 121–125 (2017)

17. Zhu, L.P., Xiao, H.M., Zhang, W.D., Yang, G., Fu, S.Y.: One-pot template-free synthesis of monodisperse and single-crystal magnetite hollow spheres by a simple solvothermal route. Cryst. Growth Des. **8**, 957–963 (2008)

18. Wang, W.W., Zhu, Y.J., Ruan, M.L.: Microwave-assisted synthesis and magnetic property of magnetite and hematite nanoparticles. J. Nanopart. Res. **9**(2007), 419–426

19. Xu, J., Yang, H., Fu, W., Du, K., Sui, Y., Chen, J., Zeng, Y., Li, M., Zou, G.: Preparation and magnetic properties of magnetite nanoparticles by sol–gel method. J. Magn. Magn. Mater. **309**, 307–311 (2007)

20. Deshpande, K., Mukasyan, A., Varma, A.: Direct synthesis of iron oxide nanopowders by the combustion approach: reaction mechanism and properties. Chem. Mater. **16**, 4896–4904 (2004)

21. de Carvalho, J.F., de Medeiros, S.N., Morales, M.A., Dantas, A.L., Carriço, A.S.: Synthesis of magnetite nanoparticles by high energy ball milling. Appl. Surf. Sci. **275**, 84–87 (2013)

22. Yazdani, F., Seddigh, M.: Magnetite nanoparticles synthesized by co-precipitation method: the effects of various iron anions on specifications. Mater. Chem. Phys. **184**, 318–323 (2016)

23. Shen, L., Qiao, Y., Guon, Y., Meng, S., Yang, G., Wu, M., Zhao, J.: Facile co-precipitation synthesis of shape-controlled magnetite nanoparticles. Ceram. Int. **40**, 1519–1524 (2014)

24. Petcharoen, K., Sirivat, A.: Synthesis and characterization of magnetite nanoparticles via the chemical co-precipitation method. Mater. Sci. Eng. B. **177**, 421–427 (2012)

25. Morato, A., Rives, V.: Comments on the application of the Scherrer equation in "Copper aluminum mixed oxide (CuAlMO) catalyst: a green approach for the one-pot synthesis of imines under solvent-free conditions". Appl. Catal. B. **202**, 418–419 (2017)

26. Hankare, P.P., Vader, V.T., Patil, N.M., Jadhav, S.D., Sankpal, U.B., Kadam, M.R., Chouguleb, B.K., Gajbhiye, N.S.: Synthesis, characterization and studies on magnetic and electrical properties of Mg ferrite with Cr substitution. Mater. Chem. Phys. **113**, 233–238 (2009)

27. Uvarov, V., Popov, I.: Metrological characterization of X-ray diffraction methods at different acquisition geometries for determination of crystallite size in nano-scale materials. Mater. Charact. **85**, 111–123 (2013)

28. McCusker, L.B., VonDreele, R.B., Cox, D.E., Louër, D., Scardi, P.: Rietveld refinement guidelines. J. Appl. Crystallogr. **32**, 36–50 (1999)

29. Jafaria, A., Shayesteha, S.F., Saloutib, M., Boustani, K.: Effect of annealing temperature on magnetic phase transition in Fe_3O_4 nanoparticles. J. Magn. Magn. Mater. **379**, 305–312 (2015)

30. Alves, A.F., Mendo, S.G., Ferreira, L.P., Mendonça, M.H., Ferreira, P., Godinho, M., Cruz, M.M., Carvalho, M.D.: Gelatine-assisted synthesis of magnetite nanoparticles for magnetic hyperthermia. J. Nanopart. Res. 18–27 (2016)

31. Legodi, M.A., de Waal, D.: The preparation of magnetite, goethite, hematite and maghemite of pigment quality from mill scale iron waste. Dyes Pigments. **74**, 161–168 (2007)

32. Upadhyay, S., Parekh, K., Pandey, B.: Influence of crystallite size on the magnetic properties of Fe_3O_4 nanoparticles. J. Alloys Compd. **678**, 478–485 (2016)

33. Tadic, M., Citakovic, N., Panjan, M., Stanojevic, B., Markovic, D., Jovanovic, D., Spasojevic, V.: Synthesis, morphology and microstructure of pomegranate-like hematite (a-Fe_2O_3) superstructure with high coercivity. J. Alloys Compd. **543**, 118–124 (2012)

34. Tadic, M., Trpkov, D., Kopanja, L., Vojnovic, S., Panjan, M.: Hydrothermal synthesis of hematite (α-Fe_2O_3) nanoparticle forms: synthesis conditions, structure, particle shape analysis, cytotoxicity and magnetic properties. J. Alloys Compd. **792**, 599–609 (2019)

35. Tadic, M., Kopanja, L., Panjan, M., Nikodinovic-Runic, J.: Synthesis of core–shell hematite (α-Fe_2O_3) nanoplates:

quantitative analysis of the particle structure and shape, high coercivity and low cytotoxicity. Appl. Surf. Sci. **403**, 628–634 (2017)

36. Jacob, J., AbdulKhadar, M.: VSM and Mössbauer study of nanostructured hematite. J. Magn. Magn. Mater. **322**, 614–621 (2010)

37. Aslibeiki, B., Ehsani, M.H., Nasirzadeh, F., Mohammadi, M.A.: The effect of interparticle interactions on spin glass and hyperthermia properties of Fe_3O_4 nanoparticles. Mater. Res. Express. **4**, 075051 (2017)

38. Ericsson, T., Krisnhamurthy, A., Srivastava, B.K.: Morin-transition in Ti-substituted hematite: a Mössbauer study. J. Phys. Scripta. **33**, 88–90 (1986)

39. Özdemir, Ö., Dunlop, D.J.: Morin transition in hematite: size dependence and thermal hysteresis. Geochem. Geophys. Geosyst. **9**, 1–12 (2008)

40. Yoshida, Y., Langouche, G.: *Mössbauer spectroscopy*, tutorial book, pp. 110–115. Springer, Fukuroi (2013)